Pyrolysis Kinetics and Combustion of Thin Wood Using Advanced Cone Calorimetry Test Method.
IN: Proceedings, 39th annual conference, North American Thermal Analysis Society, August 7-10, 2001, Des Moines, Iowa. [Online only] http://xcdsystem.com/natas2011/cdrom/search.html

Pyrolysis Kinetics and Combustion of Thin Wood Using Advanced Cone Calorimetry Test Method

Mark Dietenberger
USDA Forest Service – Forest Products Laboratory*
One Gifford Pinchot Dr.
Madison WI, USA 53705-2398
Email: mdietenberger@fs.fed.us

ABSTRACT

Mechanistic pyrolysis kinetics analysis of extractives, holocellulose, and lignin in solid wood over entire heating regime was possible using specialized cone calorimeter test and new mathematical analysis tools. Added hardware components include: modified sample holder for thin specimen with tiny thermocouples, methane ring burner with stainless steel mesh above cone heater, and water vapor sensor in heated gas sampling lines. Specialized numerical deconvolutions were applied to oxygen and water vapor analyzer signals to synchronize with rapid responding CO/CO2 analyzer signals. From this data the mass flow rates of C, H, and O within the wood volatiles as function of time were obtained, which allowed deducing mass flow rate of significant molecules of wood volatiles. Accurate analytical solution of pyrolysis kinetics was obtained for exponentially-rising, spatially-uniform temperature within the specimen as implemented in Excel spreadsheet.

INTRODUCTION

In examining past Forest Products Laboratory (FPL) research on wood pyrolysis kinetics, we choose as our starting point as the confluence of technologies achieved with thermal analysis (TGA, DSC, gas-chromatography), chemical analysis of main wood constituents, and development of inorganic salts as effective fire retardants. Through his careful measurements with grounded-up samples, FPL researcher Dr. Tang [1] in a NSF funded Ph.D. work, was perhaps the first to quantify slow pyrolysis at low temperatures and fast pyrolysis at high temperatures on a mechanistic kinetic basis for wood constituents as affected by chemical additives and oxygen concentrations. It is interesting that very low heat of combustion is associated with volatiles from low temperature slow pyrolysis, whereas high heat of combustion is associated with volatiles from high temperature fast pyrolysis. After this major work, FPL research in this field tended to deal with specific issues, such as kinetics and heat of combustion for the hemi-celluloses in addition to cellulose and lignin [2]. This work used a model-free kinetics approach that used the isoconversional method that allows for determining the dependence of effective activation energy on the extent of conversion for the isolated wood constituents. However, competition pathways could not be evaluated which limited the results to a specific transient temperature profile. More recent work was associated with finite difference models developed for wood pryolysis occurring in fires, mainly in collaboration with the universities [3]. This work provided a fair success in modeling the effect of heavy thin inert board on back side of a radiantly heated 12.5 cm thick redwood sample, in which a very significant second peak heat release rate (HRR) (and mass loss rate (MLR)) could be made to vanish by use of the inert board. It proved the Stefan-type approach to modeling wood pyrolysis in response to imposed heat flux to be inappropriate. However, the model results were not fully successful because of the lack of after-glow kinetics needed to model the oxidative gasification of final char.

Recently, voluminous biomass research provided impetus to develop ever improved estimations of wood volatiles for use in computer models. All such pyrolysis kinetics modeling found in the literature are hampered by a lack of an experimental instrument that can measure tar constituents present in primary wood volatiles as a function of time. Indeed, there are gaseous reactions, secondary tar degradations, and some repolymerization occurring within the char layer and extraction probes that prevent direct quantification of primary volatile products by any instrument. One can gain clues to such primary volatiles in specialized tests. An example is the large fraction of Levoglucosan and hydroxyacetaldehyde produced during vacuum fast pyrolysis of ground-up alpha cellulose at high temperatures and mainly simpler gases H_2O, CO, and CO_2 at low temperatures [4, 5]. Another is that the flash pyrolysis of lignin produces syringols, guaiacols, and phenols at high temperatures and mainly simpler gases of H_2O, CO, CO_2, CH_4, and CH_3OH at both low and high temperatures [5, 6]. One will even have thermal degradation of wood that produces terpenes and their byproducts as primary extractive volatiles at very low temperatures [7]. Lastly, there is the approach of tracking events within the char itself at isothermal conditions using specialized instruments such as the ^{13}C CPMAS NMR [4, 8] in which cellulose was observed to mainly remain a carbohydrate during mass loss and then gradually convert to aromatic structures with little mass losses. In spite of these developments, we note that for pyrolysis modeling there is a great need to: (1) fully account for carbon, hydrogen, and

oxygen contents of volatiles to accurately calculate the transient heat of combustion [9], (2) determine production rates of soot, H_2O, CO_2, and CO as a result of secondary tar degradations [10], and (3) develop quick procedures/methods for determining relevant, robust and inexpensive pyrolysis kinetics for various wood species and flame retardants. These factors are crucial in fire hazard modeling in CFD codes.

Another difficulty with experimental techniques associated with pyrolysis kinetics is the use of ground-up wood-constituents samples for testing [1, 5]. Although pure quantities of hemi-cellulose and alpha-cellulose has been intensively studied and accurately identified, their pyrolysis behaviors are strongly affected by the presence of various salts, moisture, and oxygen concentrations and of their physical form (crystalline versus amorphous), which are also found naturally in solid wood. As for lignin, there are continuing problems in chemically isolating a pure sample that closely resemble the actual lignin in solid wood. It is also interesting the potassium concentration affects the charring ability of the lignin [1]. Therefore, pyrolysis kinetics from measurements with an intact wood is the preferred option. We describe such an option using added cone calorimeter hardware, specialized data reduction techniques to derive primary volatile compositions as a function of time, and lastly, derive analytical solutions to the pyrolysis kinetics of terpenes, holocellulose, and lignin for the whole test time period.

ADDED CONE CALORIMETER HARDWARE

In preliminary trials, we examined how cone calorimeter testing can provide better information than achievable with the current standard, ISO5660. We used a low flame spread (FSI=70 with ASTM E84) redwood specimen, with an oven-dried density of 380 kg/m^3, in which the measured piloted-ignition surface temperature is around 361 C. One unusual redwood property is that despite a high concentration of lignin, its peak heat release rate is extraordinarily high and sharp that the simpler HRR profile functions used for the more common softwood was not appropriate [3,11]. It was also evident that considerable amount of volatiles (white smoke) occur prior to the ignition time of 19 seconds after irradiant exposure of 35 kW/m^2. We opted to construct a 75 mm-diameter manually-controlled methane ring-burner with a glowing stainless-steel screen-hat to combust the volatiles prior to gas sampling. This also ensured the development of black smoke so that we can measure by laser attenuation the concentrations of soot, which is primarily amorphous carbon. We then incorporated a high-precision, rapid-responding, full-range, relative-humidity micro-sensor (Hydrometrix HMX 2000) coupled with a thermistor temperature sensor diffused into the silicon die. The sensor as seated in a sealed stainless steel tube was inserted into the heated gas sampling line between the particle filters and the cooled moisture trap. The signal obtained with the associated palm reader (2K-PRX-HT) had a full-scale response-time of 6 seconds. The increase in relative humidity above the ambient levels is assumed due to combusting all of volatiles' hydrogen content within the sample and methane burner flames into water vapor.

Last piece of added hardware is a new sample holder developed for thin specimen mounting. Tiny Type-K thermocouples were inserted into narrow slanted crevices (cut opened with a razor blade) on both sides of the 100X100 mm specimen, and then pressed back together to ensure intimate thermocouple contacts. The thin specimen was laid on a very thin reflecting aluminum over a flat stainless steel mesh with their corners held down with thin wire clips. The effect of in-depth radiation absorption ensured a spatially uniform temperature to within 15% or less that we observed for the specimen thickness of 1.47 mm. This also allowed a very intact wood that did not distort or shrink much until well after ignition. The expelling volatiles were of enough mass flux to prevent air from penetrating the uniformly charring specimen, at least until the oxides were driven out of the developing char. This makes after-glow to be non-simultaneous with flaming, unlike that for thick specimen with deep crevices for combined combustion processes [11].

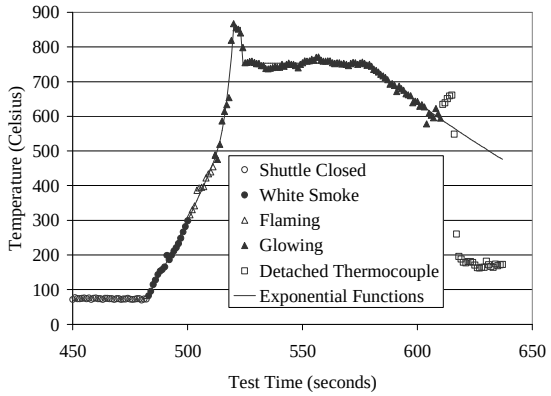

Fig. 1. Temperature profile of imbedded thermocouple in thin redwood

In Figure 1, the temperature rise of deeply imbedded thermocouple (depth of about 0.4 mm versus 0.1 mm for "surface thermocouple") was sufficiently slow to permit 35 data points (at 1 second intervals) of rapid combustible volatiles and 121 data points for slow glowing char. We note the measured temperature has an initial acceleration profile due to thermal radiation being absorbed more with the blackening of char as well as to the decreasing volumetric heat capacity associated with mass loss. Final acceleration in the temperature profile occurred at temperatures above 448 C, associated with glow combustion within the char layer [11]. The temperature then settled on a steady temperature of 753 C before it dropped during complete burnout to ashes. These glowing temperatures are sufficient to cause some sodium chloride or potassium chloride to also emerge as volatiles, as is often noted for woody biomass gasification, but is considered miniscule in the case of solid redwood used in this test.

TEST PROCEDURE AND DATA REDUCTION

Transient measurement of combustion gases and smoke to the least amount of random and systematic errors possible is necessary for pyrolysis kinetic analysis of thin materials. To assist this measurement process the nearly complete methane combustion from the ring burner was also used to re-calibrate the gas analyzers and relative humidity sensor just prior to actual specimen testing. The mass balance for incomplete combustion assumes all of (1) fuel's carbon is accounted for in the carbon dioxide, carbon monoxide, soot, and THC measurements, (2) fuel's hydrogen is accounted for in water vapor and THC measurements, and (3) fuel's oxygen is converted to become part of carbon dioxide, carbon monoxide, water vapor, and sulfur dioxide. As a basis for comparison, we have that for any incomplete hot combustion, the dynamic mass flow rate (g/s) of a fuel mixture with empirical formula $C_XH_YO_ZN_US_V$ has six equivalent calculations as derived from simple mass balances as,

$$\begin{aligned}
\dot{m}_{fuel} &= \left(\frac{12X+Y+16Z+14U+38V}{32(X+V)+8Y-16Z}\right)\left(\Delta\dot{m}_{O2}+\frac{32\dot{m}_s}{12}+\frac{16\dot{m}_{CO}}{28}+\frac{(32+8W)\dot{m}_{CHw}}{12+W}\right) \quad > Form\ 1\\
&= \left(\frac{12X+Y+16Z+14U+38V}{44X}\right)\left(\dot{m}_{CO2}+\frac{44\dot{m}_s}{12}+\frac{44\dot{m}_{CO}}{28}+\frac{44\dot{m}_{CHw}}{12+W}\right) \quad > Form\ 2\\
&= \frac{12X+Y+16Z+14U+38V}{9Y}\left(\Delta\dot{m}_{H2O}+\frac{9W\dot{m}_{CHw}}{12+W}\right) \quad > Form\ 3\\
&= \frac{12X+Y+16Z+14U+38V}{14U}\Delta\dot{m}_{N2} = \frac{12X+Y+16Z+14U+38V}{70V}\dot{m}_{SO2} \quad > Forms\ 4\ \&\ 5\\
&= \dot{m}_{CO2}+\dot{m}_s+\dot{m}_{CO}+\Delta\dot{m}_{H2O}+\dot{m}_{CHw}+\Delta\dot{m}_{N2}+\dot{m}_{SO2}-\Delta\dot{m}_{O2} \quad > Form\ 6
\end{aligned} \tag{1}$$

We implemented an improved data reduction protocol to obtain the needed agreement on the four different computations of dynamic fuel mass flow rate of methane (forms 1, 2, 3, and 6). We found signals from CO/CO_2 gas analyzer had the least errors. Time constant of their signals were quite small, about one to two seconds, which meant the cold water trap/desiccant removed the water vapor rapidly and the analyzer was optimized for fast data acquisition without sacrificing accuracy. Laser smoke signal was next in least-errors-hierarchy in that it had a similar response time, but was somewhat noisier. In addition, software time shifting in the data due to product gas arrival time at the sensors for both CO/CO_2 and laser smoke was essentially correct in corresponding with spark plug events. The paramagnetic oxygen analyzer, on the other hand, is optimized for measurement accuracy at expense of measurement speed, because of the need to measure accurately the oxygen depletion during combustion. Therefore gas-exchange volume in sensor is high relative to gas sampling flow rate, which in turn resulted in a relatively low gas flow rate in the CO_2 removal media chamber. This resulted in overall time constant of 9 seconds. Numerical deconvolution was applied to the oxygen signal to considerably reduce its response time. Since there are 4 processes (H_2O removal, CO_2 removal, sensor gas-exchange volume, and electronics delay factor) adding to overall time constant, we applied deconvolution in 4 stages assuming an exponential time response for each stage,

$$S_i(t_j) = S_{i-1}(t_j) + \tau_i\left(S_{i-1}(t_{j+1}) - S_{i-1}(t_{j-1})\right)/\left(t_{j+1}-t_{j-1}\right) \tag{2}$$

Where the index i represents the deconvolution stage level and the index j represents the time step level. Experimenting with different values of the time constant, τ_i, we have found an optimized value of 1.85 seconds for all four stages. This achieved a time response similar to the CO/CO_2 analyzer without adding undue artificial noise. A new sharper O_2 signal also meant that software time shifting of O_2 data must be reversed by 5 seconds. We have also observed a systematic error in O_2 analyzer signal due to contamination from residual CO_2 and/or H_2O byproducts in outlet gas from CO_2 removal media. Since the ambient air had minimal amount of CO_2, it was judged that oxygen calibration for zero and span was done correctly.

Therefore oxygen mole fraction must be reduced as a result of inefficient CO_2 or H_2O removal with,

$$X_{O2,corrected} = X_{O2,signal} - 0.1964 X_{CO2,signal} \qquad (3)$$

The calibrated constant was initially set to achieve agreement of total mass loss derived with that of the measured virgin wood mass minus the ash. With confidence developed in correcting the O_2 data, similar type of corrections were applied to the water vapor data. The molar H_2O fraction is essentially relative humidity as multiplied by saturation pressure and divided by atmospheric pressure. The relative humidity signal was shifted by a small amount and multiplied by a calibrated constant at low humidity levels and damped out by an exponential decay function at higher humidity levels to obtain agreement among the forms of Equation 1 and achieving the proper mass ratios of C, H, and O for when only the methane is burning. The Solver in the Excel spreadsheet was then used to further refine the calibrated constants for both oxygen depletion and relative humidity measures to ensure agreement with independent overall measures, such as the burnable mass of wood and different forms of Equation 1 while methane is only burning. Although the humidity sensor is linear throughout its measurement range, the unavoidable use of particle filters has the side-effect of absorbing moisture with relative humidity, making sensor response appear to be nonlinear. A single stage numerical deconvolution with Equation 2 using a time constant value of 3.7 seconds was found sufficient. As a last correction the H_2O data was time shifted to four seconds earlier to synchronize with the corrected O_2 and CO/CO_2 data. Since the molar fractions of O_2, CO_2, CO, and H_2O are now available and synchronized, we followed the ASTM E1354 Annex procedure for calculating the mass flow rates, respectively, of the same molecules. The soot mass flow rate is merely calculated as the smoke production rate (product of volumetric rate and extinction coefficient) divided by the specific extinction area, 8.3 m^2/g, for black smoke. These mass flow rates are then substituted into Equation 1 and the different forms of Equation 1 are shown and compared in Figure 2. During the time when the ignition shutter remained closed, the 2nd form (mainly dependent on CO_2 data) shows the least random and bias errors, while the 6th form (all mass rates equally weighted) has the most random and bias errors. All forms of fuel mass rates are in fair agreement, which help verify the added data reduction techniques. However, when the ignition shutter is open, wood pyrolysis provides the volatile "fuel" with changing and unknown compositions. This means only the sixth form (last one) of Equation 1 can be used to compare with mass loss rates measured with the load cell. Since the load cell also has a time response, we applied a single stage deconvolution using Equation 2 to weight loss data using a reasonable time constant of 2 seconds. The relatively close agreement of gas-analysis-derived fuel mass loss rates with load-cell-derived fuel mass loss rates in Figure 2 for time greater than 450 seconds validated hardware addition and data reduction improvements based on data prior to 450 seconds. A more rigorous development of this data reduction method is planned for future work.

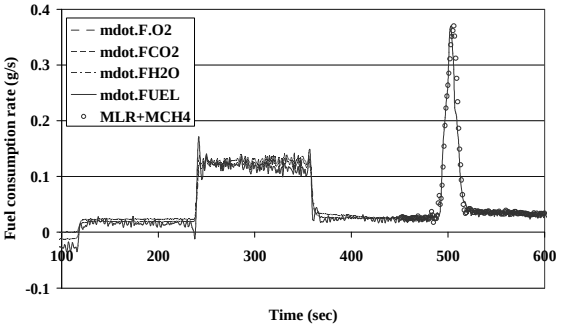

Figure 2. Comparison of fuel mass rates calculations.

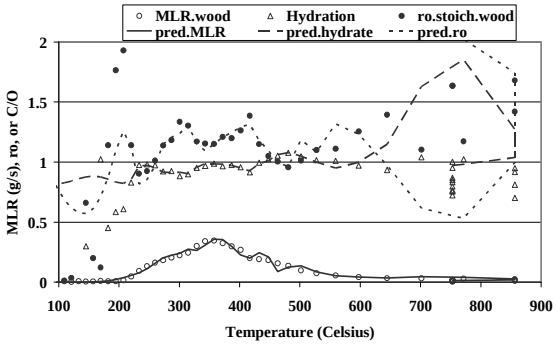

Figure 3. Trends of MLR, oxygen consumption ratio, and hydration level.

DERIVED COMPOSITIONS OF PRIMARY VOLATILES

Upon detailed examination of Equation 1, we find we can derive further properties of the fuel. Consider a volatile composition of fuel (tar), water vapor and carbon dioxide, $C_X H_Y O_Z N_U S_V + mH_2O + nCO_2$. From Equation 1, the ratio of molar carbon content of the fuel mixture to its stoichiometric molar consumption of oxygen gas is derived as,

$$\frac{\nu_{C,\,fuel}}{\Delta\nu_{O2}} \equiv \frac{X'+n}{V+X'+Y'/4-Z'/2} \cong \frac{\frac{\beta_{CO2}}{44}+\frac{\beta_s}{12}+\frac{\beta_{CO}}{28}+\frac{\beta_{CHw}}{12+W}}{\frac{\beta_{O2}}{32}+\frac{\beta_s}{12}+\frac{1}{2}\frac{\beta_{CO}}{28}+\frac{(1+W/4)\beta_{CHw}}{12+W}} \equiv \frac{8\beta_{CO2,st}}{11} \qquad (4)$$

Betas are merely the mass ratio of combustion product changes to oxygen depletion mass. We note fuel hydration level (Equation 4) is independent of water content in any form because parameter m is factored out of Equation 4. Fuel hydration levels calculated for Hydrogen Gas, Methane, Propane, Carbohydrates, Carbon Monoxide, Carbon Dioxide from Equation 4, are respectively 0, 1/2, 3/5, 1, 2, and 4 regardless of the H_2O content. Therefore, the use of fuel hydration level can assist in identifying fuel, even when combustion becomes incomplete. Suppose that during a test period, the measured

water vapor, excess nitrogen gas, sulfur dioxide, and THC's are attributed only to material pyrolysis. Using Equations 1 and 4, further fuel properties are derived as,

$$\frac{Y}{X}=\frac{Y'+2m}{X'+n}=\frac{[\dot{m}_{H2O}/9+W\dot{m}_{CHw}/(12+W)]}{\frac{\dot{m}_{CO2}}{44}+\frac{\dot{m}_s}{12}+\frac{\dot{m}_{CO}}{28}+\frac{\dot{m}_{CHw}}{12+W}}\cong\frac{[\beta_{H2O}/9+W\beta_{CHw}/(12+W)]}{\frac{\beta_{CO2}}{44}+\frac{\beta_s}{12}+\frac{\beta_{CO}}{28}+\frac{\beta_{CHw}}{12+W}} \quad (5)$$

$$\frac{Z}{X}=\frac{Z'+m+2n}{X'+n}=2+\frac{2V}{X}+\frac{Y}{2X}-\frac{11}{4\beta_{CO2,st}} \quad (6)$$

For wood, the stoichiometric net heat of combustion (kJ/g) is correlated closely as [9],

$$h_{c,st}=13.23r_o \quad , \quad (7)$$

$$r_o=(32X+8Y-16Z)/(12X+Y+16Z+14U+38V) \quad , \quad (8)$$

We note that with $HRR\approx\dot{m}''_f h_{c,st}$, piloted ignition occurred for HRR=400 kW/m^2, a high value for wood. It was also shown that r_o in virgin state is linearly related to mass fractions of extractives, holocellulose, and lignin for any wood material to a high correlation [9]. This means wood constituents should have well defined chemical makeup according to Equation 8. The holocellulose, as the major component, is made up mostly alpha cellulose, mannan, and galactan that has the empirical formula, $C_6H_{10}O_5$, while minor components are xylan and arabinan with a slightly different empirical formula. Its heat of combustion via Equation 7 is in agreement with the measured value for holocellulose [9]. An average empirical formula of lignin can be used for this paper, which is $C_9H_6O_2(H_2O)(OCH_3)_{4/3}$ using the data in Chen [13], which also has net heat of combustion via Equation 7 in agreement with that measured for the lignin [9]. In the case of extractives, monoterpenes is the main component with empirical formula, $C_{10}H_{16}$, while other observed extractives contain other derivatives of terpenes and related chemicals.

For our thin redwood test we also used "total mass loss" which is the integration of Equation 9 (introduced later) over total time to derive the total carbon, hydrogen, and oxygen mass fractions on ash free basis as the values, 0.5025, 0.0612, and 0.4363, respectively. Using the conservation of mass in conjunction with constituents' empirical chemical formulae, these translate to mass fraction values of 0.011, 0.655, and 0.334 for the extractives, holocellulose, and lignin, respectively. This compares favorably to second-growth redwood values of 0.61 and 0.33 for mass fractions of holocellulose and lignin [14]. With use of molecular weight for each empirical formula, we calculated molecular weight of redwood to be 173.9 and the basic-unit molar fractions of terpenes, holocellulose, and lignin to be $z_{terpene}$ = 0.014, z_{holo} = 0.703, and z_{lignin} = 0.283, respectively.

MOLAR FRACTIONAL RATES FOR PROPOSED PRIMARY PYROLYSIS PRODUCTS

It is interesting that Figure 3 shows significant mass losses within temperatures of 207 to 301 C prior to ignition. Since white smoke associated with wood volatiles was combusted within the methane ring burner (and replaced by black smoke), we could deduce carbon, hydrogen, and oxygen mass flow rates within the wood volatiles at all times from the mass balance equations.

$$\begin{aligned}
&\dot{m}_{C,wood}+\dot{m}_{C,methane}=\dot{m}_{SOOT}+(12/28)\dot{m}_{CO}+(12/44)\dot{m}_{CO2}\\
&\dot{m}_{H,wood}+\dot{m}_{H,methane}=(2/18)\Delta\dot{m}_{H2O}\\
&\dot{m}_{O,wood}+\dot{m}_{O,methane}=(16/28)\dot{m}_{CO}+(32/44)\dot{m}_{CO2}+(16/18)\Delta\dot{m}_{H2O}-\Delta\dot{m}_{O2}
\end{aligned} \quad (9)$$

While only the methane is burning, we can determine its C, H, and O mass flow rates, and then fixate at those flow rates during the consequential wood combustion; so that the mass flow rate of C, H, and O in the wood volatiles can be derived. Obviously, the O mass flow rates for methane from Equation 9 is theoretically zero, but for practical purposes it is not quite zero because of the various constraints on the calibrated constants for the measured gas compositions. Because the fuel hydration level was essentially zero (no carbon is being present in the volatiles) up to the temperature of 170 C, only the molar fractional rates of H_2O from holocellulose dehydration and multiplied by the molecular weight of water, 18, was fitted to the mass loss rates data in this temperature range. Then from 170 to 207 C, with fuel hydration levels oscillating between 0.5 and 1.0, the molar fractional rates of terpenes, $C_{10}H_{16}$, was also included (with its fuel hydration level as 0.71). Lastly, for rapid mass rises in the temperature range of 207 to 301 C, we included molar fractional rates of evaporated holocellulose, $C_6H_{10}O_5$. With its fuel hydration level at unity, it corresponds closely with the data. In this temperature sub-range, we now have three primary volatile molecules, which meant that we could multiply their molar fractional rates (1/s) by their

molecular weights and obtain exact agreement with the derived carbon, hydrogen, and oxygen mass flow rates from Equation 9 using the Excel spreadsheet least-squares solver in solving these following matrix equations.

$$\begin{aligned} \dot{z}_{terpene}(10*12) + \dot{z}_{holoH2O}(0) + \dot{z}_{holotar}(6*12) &= \dot{m}_{C,wood}/(m_{wood} - m_{ash}) \\ \dot{z}_{terpene}(16) + \dot{z}_{holoH2O}(4*2) + \dot{z}_{holotar}(10) &= \dot{m}_{H,wood}/(m_{wood} - m_{ash}) \\ \dot{z}_{terpene}(0) + \dot{z}_{holoH2O}(4*16) + \dot{z}_{holotar}(5*16) &= \dot{m}_{O,wood}/(m_{wood} - m_{ash}) \end{aligned} \qquad (10)$$

We constrained the solver to not allow negative values of the derived molar fractional rates. For example, if the carbon mass flow rate is zero (ie. for temperatures of up to 170 C) then molar fractional rates of terpene and holocellulose tar evaporation are derived as zeroes and molar fractional rates of protoholochar production (or holocellulose dehydrations) is derived instead as the best possible fit to mass flow rates of hydrogen and oxygen as function of time. However, if all of the mass flow rates on the right side of Equation 10 are positive, then the solver will exactly solve for molar fractional rates of evaporated terpene, dehydrated holocellulose water, and evaporated holocellulose tars, providing of course, that none of the derived molar fractional rates is negative. The resulting values for $\dot{z}_{terpene}, \dot{z}_{holoH2O}, \& \dot{z}_{holotar}$ are represented by open squares, closed triangles, and open triangles respectively in Figure 4. The integration of $\dot{z}_{terpene}$ over time is equal to the molar fraction of terpenes, as 0.01387, which makes it depleted when 301 C is reached. This high temperature of terpene depletion along with its double peak feature may be the result of high temperature rise rate that shifts kinetic processes to higher temperature, or it may be just an artifact of errors inherent within the experimental method. Nevertheless, the extractives are an established presence in the redwood, and the values derived for its emission rates are in the correct temperature range, compatible with the derived fuel hydration values, and have just enough molar fractional rates to be in agreement with its derived content in the redwood.

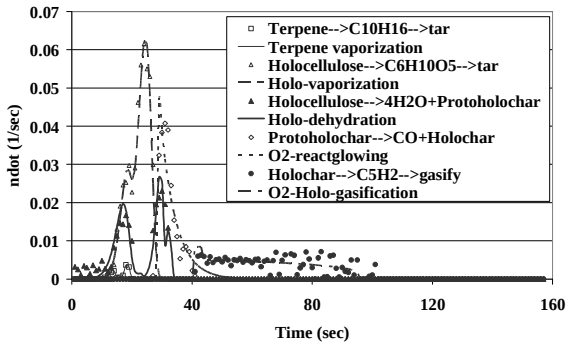

Figure 4. Modeling fractional molar rates of terpene/holocellulose.

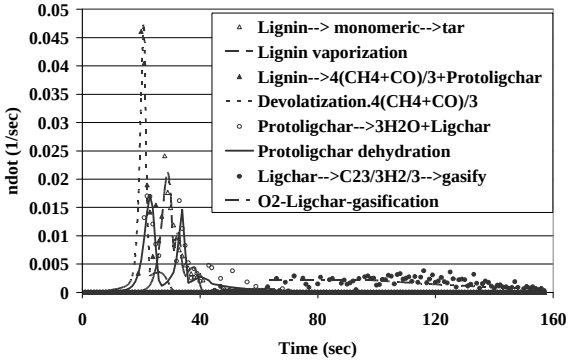

Figure 5. Modeling fractional molar rates of lignin.

The three independent set of molecules selected for the temperature range of 301 to 387 C to fit the mass flow rate data are the holocellulose basic unit of evaporation, $C_6H_{10}O_5$, lignin's charring combustible pair, (4/3)(CH_4 + CO), and the charring lignin's H_2O from its free hydroxyl group. The corresponding molar fractional rates is derived from the matrix equation as,

$$\begin{aligned} \dot{z}_{ligCH4-CO}(1.333*2*12) + \dot{z}_{ligH2O}(0) + \dot{z}_{holotar}(6*12) &= \dot{m}_{C,wood}/(m_{wood} - m_{ash}) \\ \dot{z}_{ligCH4-CO}(1.333*4) + \dot{z}_{ligH2O}(2) + \dot{z}_{holotar}(10) &= \dot{m}_{H,wood}/(m_{wood} - m_{ash}) \\ \dot{z}_{ligCH4-CO}(1.333*16) + \dot{z}_{ligH2O}(16) + \dot{z}_{holotar}(5*16) &= \dot{m}_{O,wood}/(m_{wood} - m_{ash}) \end{aligned} \qquad (11)$$

The solutions for $\dot{z}_{ligCH4-CO} \& \dot{z}_{ligH2O}$ are shown as closed triangles and open circles in Figure 5, respectively, while solution for $\dot{z}_{holotar}$ are still shown as open triangles in Figure 4. In Figure 4 we note that the holocellulose early H_2O dehydration (closed triangles) as computed with the matrix Equation 10 showed the trend of declining to zero prior to reaching 301 C as it seem to be switching over to the competing vaporization of the depolymerized alpha cellulose. The charring lignin then becomes the primary source of dehydration and is represented in the matrix Equation 11 above and shown with open circles in Figure 5. As the temperature of 402 C is reached, the alpha cellulose can no longer evaporate because by that time the hydration value is above unity, meaning that emission of CO must begin with penetration of air, which is incompatible with holocellulose vaporization. Then three independent sets of molecules chosen for temperature

range of 402 to 481 C to fit the mass flow rate data are the developing proto-holo-char's remaining H_2O and CO emissions and the lignin's evaporation of its fragmented empirical units, which is solved with the matrix equation,

$$\begin{aligned} \dot{z}_{lignintar}(10.333*12) + \dot{z}_{holoH2O}(0) + \dot{z}_{holoCO}(1*12) &= \dot{m}_{C,wood}/(m_{wood} - m_{ash}) \\ \dot{z}_{lignintar}(12) + \dot{z}_{holoH2O}(4*2) + \dot{z}_{holoCO}(0) &= \dot{m}_{H,wood}/(m_{wood} - m_{ash}) \\ \dot{z}_{lignintar}(4.333*16) + \dot{z}_{holoH2O}(4*16) + \dot{z}_{holoCO}(1*16) &= \dot{m}_{O,wood}/(m_{wood} - m_{ash}) \end{aligned} \qquad (12)$$

The solutions for $\dot{z}_{lignintar}$ is shown as open triangles in Figure 5 while $\dot{z}_{holoH2O}$ & $\dot{z}_{holoCO}$ are shown as closed triangles and open circles, respectively, in Figure 4. In this temperature range is where the 10% linear shrinking of the specimen has occurred, probably due to the crumbling lignin, but in which wire hold-downs kept the specimen flat. At the end of this temperature range, all molar fractional units of virgin holocellulose have reacted either into charring or evaporation, that is, $z_{holoH2O} + z_{holotar} = 0.703$ and final dehydrations comes to an end with $z_{holoH2O} = 0.2345$ and leaves a final carbohydrate residue (or proto-holo-char) form as C_6H_2O. In the regions where final carbohydrates have formed, the air has been penetrating to combust with the CO sites that eventually will reduce proto-holo-char further to the empirical formula of holo-char as, C_5H_2. This heat release within the char surfaces would be partially responsible for the additional acceleratory rise in the temperature observed. However, the air would not be able to penetrate the regions of fragmentating lignin, thus still preventing O_2-gasification within the lignin layers. However, the developing lignin char (or protoligchar) with the molar fraction value of z_{CH4-CO}, that is, after it has emitted 4/3(CH_4 + CO) from the phenol section and an H_2O from the propane section, will emit additional H_2O to reduce to a final dehydration form, $C_{7+2/3}H_{2/3}$,. This final H_2O production is shown as a minor change to Equation 12 within the extreme acceleratory temperature range of 481C to 856 C as the matrix equation,

$$\begin{aligned} \dot{z}_{ligtar}(10.333*12) + \dot{z}_{ligH2O}(0) + \dot{z}_{holoCO}(1*12) &= \dot{m}_{C,wood}/(m_{wood} - m_{ash}) \\ \dot{z}_{ligtar}(12) + \dot{z}_{ligH2O}(2) + \dot{z}_{holoCO}(0) &= \dot{m}_{H,wood}/(m_{wood} - m_{ash}) \\ \dot{z}_{ligtar}(4.333*16) + \dot{z}_{ligH2O}(1*16) + \dot{z}_{holoCO}(1*16) &= \dot{m}_{O,wood}/(m_{wood} - m_{ash}) \end{aligned} \qquad (13)$$

The solutions for $\dot{z}_{ligtar}$ & $\dot{z}_{ligH2O}$ are shown as the open triangle and open circle data, respectively, in Figure 5, while the solution for $\dot{z}_{holoCO}$ is shown as the open circle data in Figure 4. Alternative oxide emissions of CO or CO2 in going to a final lignin char form (or ligchar) were also examined, but could not fit the data as well as the conjectured primary H_2O emissions. The protoholochar at the end of this phase becomes depleted of its oxides when $z_{holoCO} = z_{holoH2O} = 0.2345$, leaving only the C_5H_2 sites in the holochar to gasify with the stream of incoming air. Almost simultaneously, we obtained a glowing char at which the lignin no longer is able to fragmentize and evaporate, that is, we have $z_{ligtar} + z_{ligCH4-CO} = 0.283$ for the full reaction of the virgin lignin. Without the blocking flow of volatiles from the fragmenting lignin, the inflow of air will gasify the developing ligchar with the empirical formula, $C_{7+2/3}H_{2/3}$, at high temperatures. The combined gasification processes is derived with the matrix equation,

$$\begin{aligned} \dot{z}_{holoC5H2}(5*12) + \dot{z}_{ligH2O}(0*12) + \dot{z}_{ligC23/3H2/3}((23/3)*12) &= \dot{m}_{C,wood}/(m_{wood} - m_{ash}) \\ \dot{z}_{holoC5H2}(2) + \dot{z}_{ligH2O}(2) + \dot{z}_{ligC23/3H2/3}(2/3) &= \dot{m}_{H,wood}/(m_{wood} - m_{ash}) \\ \dot{z}_{holoC5H2}(0*16) + \dot{z}_{ligH2O}(1*16) + \dot{z}_{ligC23/3H2/3}(0*16) &= \dot{m}_{O,wood}/(m_{wood} - m_{ash}) \end{aligned} \qquad (14)$$

Solution for $\dot{z}_{holoC5H2}$ is shown as closed circles in Fig. 4, while solutions for $\dot{z}_{ligH2O}$ & $\dot{z}_{ligC23/3H2/3}$ are shown as open and closed circles, respectively, in Figure 5. Note that after several seconds of gasification, the protoligchar becomes fully dehydrated as ligchar with the empirical formula, $C_{7+2/3}H_{2/3}$, at the molar fraction value of $z_{ligH2O} = z_{ligCH4-CO} = 0.1539$. It is interesting that during the acceleratory temperature rise, that the hydration values are sufficiently above unity (see Figure 3) to imply fast reactions with the CO sites in the protoholochar; but that during the consequential "constant" high temperatures, the hydration values are sufficiently below unity to indicate the dominance of holochar gasification over that of ligchar gasification. We speculate the higher hydrogen concentrations derived for the holochar makes it relatively more reactive during gasification. At around 56 seconds before the end of the test, the holochar becomes fully gasified when $z_{holoC5H2} = z_{holoCO} = z_{holoH2O} = 0.2345$. Remaining mass loss is accomplished by ligchar gasification which ends at, $z_{ligC23/3H2/3} = z_{ligH2O} = z_{ligCH4-CO} = 0.1539$, right at the end of the test. We observed that once the constant temperature of 752 C is reached, there was no longer any need for significant H_2O, CO, or other simple emitting gases to maintain low values

of r_o, because its measured value (not shown in Figure 3), despite its high level of noise, is like that of amorphous carbon as 2.667.

It is interesting that to obtain reasonable fit to the data during glow combustion we needed to postulate O_2-gasification occurring in three stages, by firstly involving a fast reaction to cause the release of CO from the protoholochar, secondly with the hydrocarbon holocellulose char (holochar), and thirdly with nearly graphitic remains of lignin char (ligchar). It is gratifying to derive the single peaks for the major constituents' partial evaporation of hemicellulose, alpha cellulose, and lignin as occurring in their proper temperature ranges. However, the early and late peaks of water vapor production during dehydration for both holocellulose and lignin was required to achieve the low values of r_o observed during the constituents' partial monomeric evaporation. Because we required mass conservation of carbon, hydrogen, and oxygen mass content of the wood specimen at all times as well as conserving molar production pertaining to the major constituents, meant that all phases of pyrolysis processes must be carefully modeled to prevent distortions on the whole system, and in such a manner that several different peaks can occur to allow the mechanistic kinetics based analysis for each proposed molecule emission.

TERPENES KINETIC ANALYSIS

The derived molar-fractional-rates of terpenes as function of time in Figure 4 has a double peak feature covering the temperature range, 170 to 301 C, suggesting dual-stage kinetics. We note that the total area under both peaks is equal to the molar fraction of terpenes, as 0.01387. Consider the single-order dual-stage Arrhenius-kinetics reaction for the terpene vaporization (tv) as,

$$\dot{z}_{tv,i}(t) = \left(f_{tv,i} - z_{tv,i}(t)\right) A_{tv,i} \exp(-E_{tv,i} / RT) \tag{15}$$

$$0.01387 = \sum_i f_{tv,i} \tag{16}$$

Solving Equation 15 analytically, we obtained,

$$z_{tv,i}(t) = f_{tv,i}\left[1 - \exp\left(-A_{tv,i} I_{tv,i}(t)\right)\right] \tag{17}$$

$$I_{tv,i}(t) = \int_0^t \exp(-E_{tv,i} / RT)\, dt \tag{18}$$

To use Equation 15 directly and conveniently in a spreadsheet, requires that the integral expression given by Equation 18 be evaluated for any value of time. Since Figure 1 shows a single fitted exponential temperature rise from 75 to 448 C within 28 seconds, the expression for each temperature range is,

$$T(t) = T(t_k) + a_k\left[\exp\left(b_k (t - t_k)\right) - 1\right] \quad . \tag{19}$$

The solution to the integral in Equation 18 using the inverted form of Equation 19 is then,

$$I_{tv,i}(t) = I_{tv,i}(t_k) + \frac{1}{b_k}\left\{\exp\left(\frac{E_{tv,i}}{R\left(a_k - T(t_k)\right)}\right)\int_{y_k}^{y}\frac{\exp(-s)ds}{s} - \int_{x_k}^{x}\frac{\exp(-s)ds}{s}\right\} \tag{20}$$

$$y = x + \frac{E_{tv,i}}{R(a_k - T(t_k))} = \frac{E_{tv,i}}{R}\left(\frac{1}{T(t)} + \frac{1}{a_k - T(t_k)}\right) \quad . \tag{21}$$

To within 0.015% error at about x =1 and much less error everywhere else, we derived the formula,

$$\int_x^{\infty}\frac{\exp(-s)ds}{s} = \exp(-x)\cdot\ln\left[1 + \frac{1}{x}\left(\frac{x^4 + 4.4842x^3 + 3.6044x^2 + 0.4723x + 0.005377}{x^4 + 4.9841x^3 + 4.9443x^2 + 0.7942x + 0.009577}\right)\right] \tag{22}$$

We note that the variable y must be kept positive, implying that the term, $a_k - T(t_k)$, must be kept positive. With only a few intervals of temperature fitting in Figure 1, it was simple to incorporate solution of Equation 18 over the whole test time for any proposed reaction through a call to our VBA subroutines in the Excel spreadsheet. Activation energy of any reaction, $E_{xy,i}$, and time, t ,are the only inputs to the routine and the output is the value for Equation 18. The very good fit of Equation 15 to the derived terpenes evaporation data $\dot{z}_{terpene}$ is shown in Figure 4 and derived kinetics parameters are listed in Table 1 as the "tv" row. It is seen that this analytical approach is tolerant of rapid changes or even scarcity in the experimental data without having to resort to the very short time stepping required in a numerical integration of Equation 18. Indeed, the availability of the highly precise approximation given by Equation 22 also permits several other analytical expressions to be used for the temperature as function of time.

Table 1 Arrhenius parameters for wood constituents: terpenes, holocellulose, and lignin.

Process xy[a]	$f_{xy,1}$	$A_{xy,1}$ **1/s**	$E_{xy,1}$ **kJ/mol**	$f_{xy,2}$	$A_{xy,2}$ **1/s**	$E_{xy,2}$ **kJ/mol**
tv	0.00558	2.097E+18	171	0.00836	2.956E+25	268
hc	0.39018[c]	2.945E+02	52	0.31302[c]	2.912E+06	72
hv	0.39018[c]	9.7494E+07	102	0.31302[c]	1.285E+10	112
hd	0.13768	6.18E+11	128	0.86232	4.60E+15	215
hr	1.0	0.2	0.0001	--	--	--
hg	1.0	1.7	47	$n_{hg,1} = 0.2$	--	--
lc	0.11066	2.995E+19	218	0.15667[c]	6.654	28
lv	0.01553	1.9059E+03	57	0.15667[c]	1.8593E+12	169
ld	0.46327	8.4222E+10	132	0.06688	2.93E+13	195
ld,3[b]	0.46985	0.82491	20	--	--	--
lg	1.0	7.40E-02	30	$n_{lg,1} = 0$	--	--

[a]Replace "xy" by appropriate characters below it in the table (see text for definitions)
[b]Lignin has three stages for dehydration
[c] Competing processes of vaporization (v) and charring (c) which share the constituents molar fraction.

HOLOCELLULOSE KINETIC ANALYSIS

In Figure 4, if we focused on competing reactions between early dehydration and evaporation of monomeric units, it is apparent there are two peaks of H_2O fractional molar flow rate as well as two peaks of holocellulose evaporation fractional molar flow rate. A sharp demarcation between groups of holocellulose subunits is not possible, requiring us to consider first-order dual-staging with competing reactions fitted to the data as follows.

$$\dot{z}_{hc,i}(t) = \left(f_{h,i} - z_{hc,i}(t) - z_{hv,i}(t)\right)A_{hc,i}\exp(-E_{hc,i}/RT) \quad (23)$$

$$\dot{z}_{hv,i}(t) = \left(f_{h,i} - z_{hv,i}(t) - z_{hc,i}(t)\right)A_{hv,i}\exp(-E_{hv,i}/RT) \quad (24)$$

$$0.7031 = \sum_j f_{h,j} \quad (25)$$

$$z_{hc,i}(t) + z_{hv,i}(t) = f_{h,i}\left[1 - \exp\left(-A_{hc,i}I_{hc,j}(t) - A_{hv,i}I_{hv,i}(t)\right)\right] \quad . \quad (26)$$

Thus for j=1, Equation 23 represents charring reaction (hc,1) for low-temperature holocellulose units (h,1) (monomeric portions of hemicellulose and amorphous alpha cellulose) while Equation 24 represents the competing reaction for evaporation (hv,1) of also the low-temperature holocellulose units (h,1), and for j=2, Equation 23 represents charring reaction (hc,2) for high-temperature holocellulose units (h,2) (monomeric portions of crystalline alpha cellulose) while Equation 24 represents the competing reaction for evaporation (hv,2) of high-temperature holocellulose units (h,2). Equation 25 provides the molar fraction value for the holocellulose while Equation 26 is the analytical solution to the sum of Equations 23 and 24. A factor, $e = 0.5329$, is the fraction of holocellulose dehydrations that is directly involved in the charring reactions competing with evaporation reactions. To put in another way, the number of H_2O produced per monomeric unit during early dehydration is derived to be $4e = 2.1316$. To accommodate this factor, the spreadsheet solver was set up to obtain the simultaneous least-squares solutions of the sum $e*(\dot{z}_{hc,1} + \dot{z}_{hc,2})$ as a fit to the data $\dot{z}_{holoH2O}$ in the early dehydration regime and of the sum $\dot{z}_{hv,1} + \dot{z}_{hv,2}$ as a fit to the data $\dot{z}_{holotar}$. In this way the Equation 25 remains valid. The overall fit is shown in Figure 4 as the early dehydration and vaporization curves. The derived kinetic values are listed in Table 1 as the "hc" and "hv" rows. The activation energies of dehydration, denoted as $E_{hc,j}$, are much lower than the activation energies of evaporation, denoted as $E_{hv,j}$, meaning that at low temperatures or low temperature rise rate, the charring reaction dominates, whereas at high temperature along with high rise rate, holocellulose almost completely evaporate.

Indeed, using the values in Table 1, we can determine the transition temperatures at which the dehydration reactions are superceded by the vaporization reactions. That is, from $\dot{z}_{hc,1} = \dot{z}_{hv,1}$, the transition temperature is 200 C, just as is expected for hemicellulose and amorphous alpha cellulose. Likewise, from $\dot{z}_{hc,2} = \dot{z}_{hv,2}$, the transition temperature is 300 C, just as is expected for crystalline alpha cellulose. Therefore, if one heats the holocellulose quickly to some low temperature between 100 and 200 C in inert gases, the reaction is solely dehydration and ultimately the char will have the empirical formula,

C_6H_2O, which is a char mass fraction value of 0.555. If instead one heats the holocellulose quite rapidly to temperatures just below 300 C, then its char mass fraction is instead about 0.555*0.313/(0.313+0.39) = 0.247, due to degradation of hemicellulose and amorphous alpha cellulose by depolymerization and vaporization. Of course, flash heating of holocellulose to temperatures greatly above 300 C, will result in complete vaporization, and no char will remain. The required heating rates cannot be realistically obtained, but this simple calculation exercise indicates the flexibility of the current kinetics model in predicting various behaviors of wood degradation not captured by a simpler kinetics model, such as those discussed in the Introduction section.

The ultimate dehydration (hd) for the remaining $4(1-e)=1.8684$ units of H_2O per monomeric char unit is modeled as single-order dual staging reaction as,

$$\dot{z}_{hd,i}(t) = \left(z_{hd,i}(\infty) - z_{hd,i}(t)\right) A_{hd,i} \exp(-E_{hd,i} / RT) \quad (27)$$

$$z_{hd,i}(\infty) = f_{hd,i} \sum_j z_{hc,j}(t) \quad (28)$$

$$1 = \sum_i f_{hd,i} \quad (29)$$

Analytical integration of Equation 27 is similar to Equation 17. Note that Equation 28 describes the availability of cross-linked-carbon protoholochar as function of time, which with the temperature history in Figure 1 it becomes an upper limiting value by the time ultimate dehydration begins. The sum $(1-e)(\dot{z}_{hd,1} + \dot{z}_{hd,2})$ is fitted with the Solver in a least-squares method to the data $\dot{z}_{holoH2O}$ at high temperatures (above 401 C) and is shown in Figure 4 as the second main feature of the dehydration curve. The corresponding kinetics parameters are listed in Table 1 as the "hd" row. After ultimate dehydration the protoholochar has empirical formula, C_6H_2O, which in order to continue to fit our data it must gasify CO with penetrating O_2 and then lastly gasify the resulting holochar, C_5H_2. Kinetics equations for the gasifications are,

$$\dot{z}_{hr,i}(t) = \left(z_{hr,i}(\infty) - z_{hr,i}(t)\right) A_{hr,i} \exp(-E_{hr,i} / RT) \quad (30)$$

$$z_{hr,i}(\infty) = f_{hr,i} \sum z_{hc,j}(t) \quad (31)$$

$$1 = \sum_i f_{hr,i} \quad (32)$$

$$\dot{z}_{hg,i}(t) = \left(z_{hg,i}(\infty) - z_{hg,i}(t)\right)^{n_{h,j}} A_{hg,i} \exp(-E_{hg,i} / RT) \quad (33)$$

$$z_{hg,i}(\infty) = f_{hg,i} \sum z_{hc,j}(t) \quad (34)$$

$$1 = \sum_i f_{hg,i} \quad (35)$$

Solution for Equation 33 for when the reaction is not first orders (that is, $n_{h,j} \neq 1$), is a power expression,

$$(z_{hg,j}(\infty) - z_{hg,j}(t))^{(1-n_{h,j})} - (z_{hg,j}(\infty))^{(1-n_{h,j})} = (n_{h,j} - 1) A_{hg,j} [I_{hg,j}(t) - I_{hg,j}(t_o)] \quad (36)$$

Otherwise it is the exponential expression similar to Equation 17 and that also with Equation 30. Derived kinetics parameters are in Table 1 as "hr" and "hg" rows and the fit to the data is shown in Figure 4 as the O_2-reactglowing curve, $\dot{z}_{hr,1}$, comparing with the open circle data and O_2-gasification curve, $\dot{z}_{hg,1}$, comparing with closed circle data. We obtained analytical solutions to these equations since the penetrating O_2 begins only after holocellulose has finished with evaporation and thus we set the initial time as, $t_o = 28\ s$. The best modeling of the CO emission was to consider first-order single stage kinetics with nearly zero activation energy, and is labeled as "react-glowing". This material is labeled as "reactglonite" to distinguish it from other types of protoholochar, such as the cured charcoal that does not self-heat upon contact with air. When the reactglowing is completed the resulting holochar has a regular O2-gasification reaction that requires a quite low-order single-stage reaction, $n_{hg,1} = 0.2$, with also a low activation energy of $E_{hg,1} = 47$ kJ/mol to provide a very broad peak for glowing from 40 to 100 seconds in Figure 4.

LIGNIN KINETIC ANALYSIS

Recall that Figure 5 shows the derived fractional molar rates for various proposed processes of lignin degradation. The volatile emissions of 4/3(CH_4+CO) or demethoxylization and decarbononization that result in charring of the lignin "lc" is shown as closed triangles in partial competition with evaporation of lignin basic units "lv" as open triangles. With these processes occurring over a wide temperature range, three stages of first-order reactions, with competition only for the "middle temperature" stage reaction, were modeled with the equations,

$$\dot{z}_{lc,1}(t) = \left(f_{lc,1} - z_{lc,1}(t)\right) A_{lc,1} \exp(-E_{lc,1} / RT) \quad (37)$$

$$\dot{z}_{lv,1}(t) = \left(f_{lv,1} - z_{lv,1}(t)\right) A_{lv,1} \exp(-E_{lv,1} / RT) \quad (38)$$

$$\dot{z}_{lc,2}(t) = \left(f_{l,2} - z_{lc,2}(t) - z_{lv,2}(t)\right) A_{lc,2} \exp(-E_{lc,2} / RT) \quad (39)$$

$$\dot{z}_{lv,2}(t) = \left(f_{l,2} - z_{lc,2}(t) - z_{lv,2}(t)\right) A_{lv,2} \exp(-E_{lv,2} / RT) \quad (40)$$

$$0.2829 = f_{lc,1} + f_{lv,1} + f_{l,2} \quad (41)$$

The analytical solutions to Equations 37 and 38 are similar to Equation 17, while the analytical solution to the sum of Equations 39 and 40 is similar to Equation 26. As fits to the data in Figure 5, the charring of lignin is indicated by the devolatization curve shown as dotted lines and the fragmentation/evaporation of lignin is indicated by the vaporization curve shown as dashed lines. The corresponding kinetic parameters are given in Table 1 as the "lc" and "lv" rows. The first event in lignin degradation as devolatization is modeled with the non-competitive Equation 37 and is shown as the first large peak of the dotted curve. The supposed crosslinking of the carbon during this reaction ensures the survival of the resulting protoligchar for eventual dehydration to become a ligchar. The secondary smaller peak of the dotted devolatization curve is modeled with the Equation 39 which is in competition with Equation 40. The next main event in lignin degradation, as fragmentation, is modeled with Equation 40 in competition with Equation 39 and is shown as the first and second peak of the dashed curve. The transition temperature from secondary devolatization to fragmentation as computed from the equality, $\dot{z}_{lc,2} = \dot{z}_{lv,2}$, is 370 C, which corresponds to the known breaking apart of lignin's carbon atoms. Finally, any pockets of lignin resistant to lower temperature devolatization or fragmentation is forced to fragment at the high temperatures generated from protoholchar's reactglowing and is predicted by Equation 38 as the smaller dashed peak from 35 to 41 s.

The lignin char units formed from the completion of devolatization has the empirical formula, $C_{7+2/3}H_{4+2/3}O_2(H_2O)$, at a molar fraction value equal to z_{CH4+CO}. In a triple-stage dehydration process this protoligchar unit will emit $3H_2O$, shown as the closed triangles, reducing it to the ligchar, $C_{7+2/3}H_{2/3}$. This is modeled by the kinetic equations,

$$\dot{z}_{ld,i}(t) = \left(z_{ld,i}(\infty) - z_{ld,i}(t)\right) A_{ld,i} \exp(-E_{ld,i} / RT) \quad (42)$$

$$z_{ld,i}(\infty) = f_{ld,i} \sum_j z_{lc,j}(t) \quad (43)$$

$$1 = \sum_i f_{ld,i} \quad (44)$$

The solution to Equation 42 is similar to Equation 17 and the kinetic parameters are given in Table 1 as "ld" and "ld,3" row. The predictions are shown as the solid curves in Figure 5 as a comparison to the open circle data. It is evident there are three peaks of dehydration predicted for the protoligchar. The third peak of dehydration seemed questionable given the noise level of the open circle data during the constant temperature phase of glowing. However, the other alternative of releasing CO from the protoligcchar as the analogy to reactglowing in the protoholochar was found in the previous section as not providing as good as agreement with the data as was the release of H_2O. The graphitic gasification of ligchar as shown broadly from 63 to 157 s seemed to be adequately modeled by a zeroth-order single stage reaction with the equation,

$$\dot{z}_{lg,i}(t) = \left(z_{lg,i}(\infty) - z_{lg,i}(t)\right)^{n_{l,j}} A_{lg,i} \exp(-E_{lg,i} / RT) \quad (45)$$

$$z_{lg,i}(\infty) = f_{lg,i} \sum z_{lc,j}(t) \quad (46)$$

$$1 = \sum_i f_{lg,i} \quad (47)$$

The solution to Equation 45 is similar to Equation 36. The predicted ligchar gasification is shown as dashed-dotted line in Figure 5 and the corresponding kinetic parameters are in Table 1 as the "lg" row. Despite quite low activation energy, the presence of oxygen gas in char layer is still required for the reactions.

CONCLUSION

In this paper we described a procedure to derive the mechanistic pyrolysis kinetics of extractives, hololcellose, and lignin from their fit to mass rate production of C, H, and O within wood volatiles produced in a modified cone calorimeter testing of thermally thin redwood specimen. To increase the accuracy of cone calorimeter testing we applied numerical deconvolutions to signals from Oxygen analyzer, relative humdidity sensor, and load cell. To eliminate white smoke as well as recalibrate the O_2 analyzer and RH sensor, we installed a methane ring burner above the cone heater and compared alternate calculations of methane mass flow rates. This was sufficient to provide reliable mass loss rates, oxygen consumption ratios, and fuel hydration level as function of time for the wood specimen. The 35 kW/m^2 radiant heating of 1.47 mm thick intact redwood on a modified holder provided an optimum temperature rise-rate along with a relatively uniform temperature within the specimen, such that all significant pyrolysis mechanisms could be observed as a function of temperature.

Under the particular conditions of this single test, it was derived that one-third of holocellulose charred while the other two-thirds of the holocellulose evaporated; and that 54% of the lignin charred while the other 46% of lignin evaporated. With sophisticated kinetic modeling described in this paper, it was possible to compute the change in these ratios for alternative conjectured temperature profile conditions that gave reasonable values of char production. It was also possible to derive rates of oxides emission and char gasification by O_2 at very high temperatures and to fit them with analytical solutions of kinetic equations in both acceleratory and constant temperature conditions. In particular, the O_2-gasification and heat-releasing oxidation of CO sites in the dehydrated holocellulose char (labeled as protoholochar) was found to be best modeled with vanishing activation energy, prompting us to label it as reactglowing and the corresponding material as reactglonite. However, with improved future instrumentation and data analysis this interesting feature could be modified. It is interesting that once the various primary volatile molecules were reasonably quantified for both holocellulose and lignin by a deduction process that the complete set of kinetic equations, but with different values for the parameters, are somewhat similar for both constituents.

Because of the insistence on conserving C, H, and O mass rates in the wood volatiles at each step of time with the kinetics model, the added feature is the simultaneous predictions of mass loss rates, heat of combustion, and hydration values as a function of time and be also adaptable to alternative temperature profiles, which we plan to test in a thick pyrolysis model [2]. No other reported kinetics models to our knowledge has this capability, except the crude kinetics model described in our earlier paper [9]. Furthermore, we report here for the first time the various analytical solutions to the kinetic equations with challenging temperature profiles. Since the salt-based fire retardants and changing the wood species alter the kinetic processes, it would be obvious to extend the method described in this paper for these situations. Other recommendations would be a yet better design for a modified cone calorimeter test. One design change would be a better and prior calibration of gas analyzers and sensors through combusting pure ethylene glycol in a 100 mm by 100 mm holder pan. A more rigorous statistical analysis can fine tune the various stages of this valid pyrolysis kinetic analysis.

REFERENCES

1. Tang, W., "Effect of Inorganic Salts on the Pyrolysis, Ignition, and Combustion of Wood, Cellulose, and Lignin", Ph.D. Thesis, Chemical Engineering, University of Wisconsin – Madison, 1964, 275pp.
2. Parker, W. and LeVan, S., "Kinetic Properties of the Components of Douglas-Fir and Heat of Combustion", Wood and Fiber Sci. 21(3), 1989, pp. 289-305.
3. Hagge, M., Bryden, K., and Dietenberger, M., "Effect of Backing Board Materials on Wood Combustion Performance", *Proc. Wood & Fire Safety, 5th Int. Scientific Conference*, Technical Univ. of Zvolen, Slovakia, April, 2004.
4. Shafizadeh, F., "The Chemistry of Pyrolysis and Combustion", *The Chemistry of Solid Wood*, Rowell R. (ed.), Advances in Chemistry Series -207, American Chemical Society, Washington, D.C., 1984, pp. **13**/489-529.
5. Muller-Hagedorn, M., Bockhorn, H., Krebs, L., and Muller, U., "A Comparative Kinetic Study on the Pyrolysis of Three Different Wood Species", *J. Anal. Appl. Pyrolysis*, **68-69**, (2003), pp. 231-249.
6. Avni, E., Davaudsadeh, F., and Couglin, R., "Flash Pyrolysis of Lignin", *Fundamentals of Biomass Thermochemical Conversion*, Overend, Milne, and Mudge, (eds.), Elsevier, London, 1985, pp. 329-343.
7. McGraw, G., Hemingway, R., Ingram, L., Canady, C., and Mcgraw, W., "Thermal Degradation of Terpenes: Camphene, A-Carene, Limonene, and a-Terpinene", *Environ. Sci. Technol.*, **33**, 1999, pp. 4029-4033.
8. Wooten, J.B., Seeman, J.I., and Hajaligol, M.R., "Observation and Characterization of Cellulose Pyrolysis Intermediates by ^{13}C CPMAS NMR, A New Mechanistic Model", *Energy & Fuel*, **18**(1), Feb. 2004, 1-15.
9. Dietenberger, M., "Update for Combustion Properties of Wood Components", *Fire & Materials J.*, **26**, 2002, pp. 255-267.
10. Boroson, M., Howard, J., Longwell, J., and Peters, W., "Product Yields and Kinetics from the Vapor Phase Cracking of Wood Pyrolysis Tars", *AIChE J.*, **35/1**, January, 1989, pp. 120-128.
11. Dietenberger, M., "Effect of Backing Board on the Heat Release Rate of Wood", *Proc. Intl. Conf. on Fire Safety*, Hilado, C. (ed.), July 1999, Columbus, OH.
12. DeGroot, W. and Richards, G., "Gasification of Cellulosic Chars in Oxygen and in Nitrogen Oxides", *Carbon*, **29/2**, (1991), pp. 179-183.
13. Chen, C., "Lignins: Occurrence in Woody Tissues, Isolation, Reactions, and Structure", *Wood Structure and Composition*, Lewin and Goldstein, (eds.), Marcel Dekker, Inc, New York, 1991, pp 183-261.
14. Pettersen, R., "The Chemical Composition of Wood", *The Chemistry of Solid Wood*, Rowell R. (ed.), Advances in Chemistry Series -207, American Chemical Society, Washington, D.C., 1984, pp. 2/57-126.
15. Lewellen, P., Peters, W., and Howard, J., "Cellulose Pyrolysis Kinetics and Char Formation Mechanism", *16th Sym. On Combustion*, August 1976, pp.1471-1480.
16. Drews, M. and Barker, R., "Pyrolysis and Combustion of Cellulose Part VI. The Chemical Nature of the Char", *Pyrolysis of Polymers, Vol. 13, Fire and Flammability Series*, Hilado, C. (ed.), Technomic Publishing, 1974, pp. 21-29.
17. Kollmann, F. and Topf, P., "Exothermic Reactions of Wood at Elevated Temperatures", *Pyrolysis of Polymers, Vol. 13, Fire and Flammability Series*, Hilado, C. (ed.), Technomic Publishing, 1974, pp. 43-51

NATAS North American Thermal Analysis Society

Technical Program of the 39th

NORTH AMERICAN THERMAL ANALYSIS SOCIETY CONFERENCE

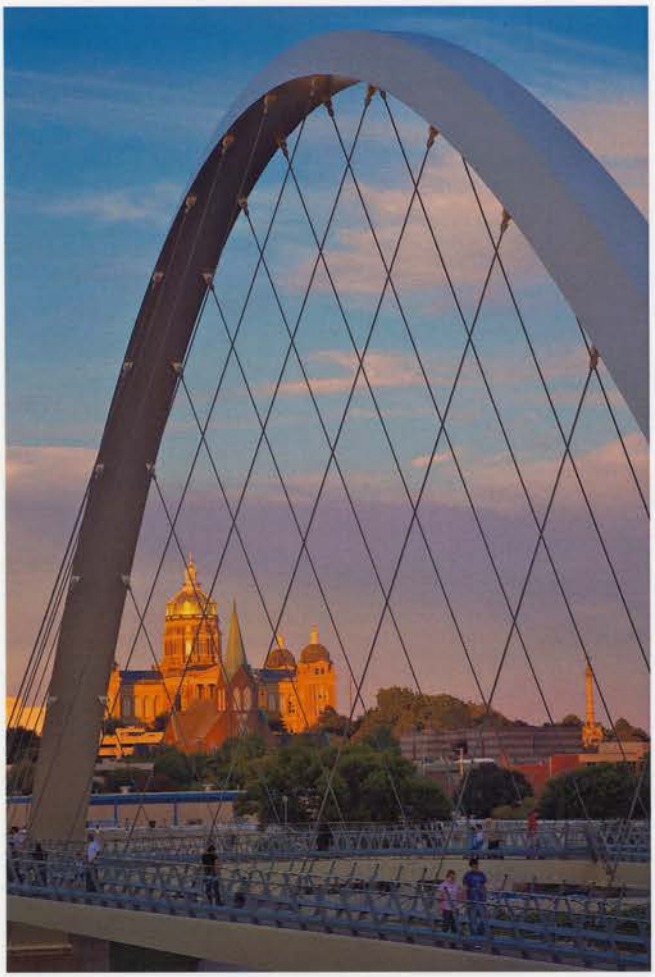

August 7–10, 2011

Des Moines Downtown Marriott
Des Moines, Iowa

NATAS North American Thermal Analysis Society

TECHNICAL PROGRAM OF THE 39TH NORTH AMERICAN THERMAL ANALYSIS SOCIETY CONFERENCE

August 7–10, 2011

Des Moines Downtown Marriott
Des Moines, Iowa

Conference Chair
Michael Kessler
Iowa State University

Technical Program Chair
Prashanth Badrinarayanan
Iowa State University

Short Course Chair
Larry Judovits
Arkema, Inc.

Vice-Chair, Exhibits
Bob Fidler
NETZSCH Instruments N.A. LLC

NATAS Meetings Councilor
Bob Howell
Central Michigan University

NATAS Staff Management
Lois Hall
Western Kentucky University

Proceedings Editor
Diana S. Smirnova
ExxonMobil Research and Engineering

Proceedings Assistant Editors
K. F. Schoch, Jr., Northrop Grumman Corp.
Queenie Kwok, Canadian Explosives Research Laboratory

Table of Contents

 Additional copies of NATAS 2011 conference abstracts and papers can be obtained by contacting: NATAS c/o Thermal Analysis Laboratory, Western Kentucky University, The Center for Research and Development, 2413 Nashville Road, Bowling Green, KY 42101. Phone: 270-745-2220, Fax: 270-745-2221, Email: natas@wku.edu.

Printed by X-CD Technologies, Toronto, Ontario, Canada, www.x-cd.com

Cover and CD photo by Larry Lindell, courtesy of the Greater Des Moines Convention & Visitors Bureau.